JASA ARTICLE

The influence of fluid boundary conditions on bio-inspired acoustic flow sensor

Morteza Karimi,[1,a)] Junpeng Lai,[1] Weili Cui,[2] Changhong Ke,[1] and Ronald N. Miles[1,b)]
[1]Department of Mechanical Engineering, Binghamton University, Binghamton, New York 13902, USA
[2]Department of Mechanical & Facility Engineering, School of Engineering, SUNY Maritime College, Bronx, New York 10465, USA

ABSTRACT:
One common approach to creating a flow sensor is to fabricate sensing elements that extend perpendicularly from the substrate, which typically provides sensor anchorage. However, this approach is impractical due to fabrication challenges, structural fragility, and integration constraints. This paper explores an alternative packaging method that integrates the sensor into a silicon chip for protection. Since this integration introduces boundary conditions from the substrate, which negatively affect sensor performance, the substrate is removed to modify the fluid boundary condition by transferring the sensing element to a designed cavity (3400 μm length, 1690 μm width, and 500 μm depth). This process eliminates surrounding material while preserving the sensor element for comparison before and after substrate removal. To illustrate this effect, the study presents examples that, while not optimized as flow sensors, could still demonstrate how boundary conditions influence sensor performance. Results indicate that removing the substrate increases viscous damping due to air interaction while reducing damping from substrate boundaries. This leads to lower pressure-referred noise levels and a higher signal-to-noise ratio. These findings could be useful for alternative packaging methods, where the substrate beneath the sensor is completely removed through back-etching. This approach provides protection while simultaneously preserving sensor performance.
 https://doi.org/10.1121/10.0036459

(Received 2 September 2024; revised 1 March 2025; accepted 1 April 2025; published online 21 April 2025)

[Editor: Thomas Edward Blanford] Pages: 3045–3056

I. INTRODUCTION

Microcantilever beams have demonstrated their effectiveness in detecting minute flow variations across various applications,[1–5] with their performance being heavily dependent on material properties.[6,7] However, the inherent thermal noise floor, which determines the minimum detectable signal, poses a significant obstacle to the performance of micromechanical sensors, masking weak signals and limiting their efficacy.[8–14] Therefore, optimizing design parameters, such as adjusting the viscous damping around the flow sensor, is crucial for achieving a low-noise microscale flow sensor. In this article, an attempt is made to demonstrate the strong dependence of the thermal noise floor and acoustic response on viscous damping and how changing the fluid boundary conditions around the flow sensor can alter the viscous force. This, in turn, helps decrease the pressure-referred noise (PRN) level and design a better flow sensor.

In microphone design, it is well established that the power spectral density of thermal noise floor is directly proportional to the damping. This relationship is expressed as $G_{PP} = K_b T C/\pi\ S_d^2$.[15] Here, G_{PP} represents the PRN (Pa^2/Hz), K_b the Boltzmann constant (J/K), T the temperature (K), C the damping coefficient (Ns/m), and S_d the diaphragm area (m). Damping can have both positive (good damping) and negative (bad damping) effects on device performance. Designers face limited options for addressing thermal noise floor issues in pressure-sensing microphones, typically focusing on reducing viscous damping or increasing the diaphragm area.[15,16] However, the pursuit of either of these options can have adverse consequences, potentially impacting production costs and other performance metrics. Such an issue becomes more severe for smaller microphones fabricated using micro-electromechanical systems technology, which are typically more vulnerable to thermal noise than larger microphones. In contrast, in innovative microphone designs that prioritize sensing fluid motion over sensing pressure, damping takes on a distinctly important role. Enhanced damping might be advantageous in such designs to enhance the sensor's responsiveness to acoustic signals and bolster the signal-to-noise ratio. Consequently, while damping plays a crucial role in mitigating noise and preserving signal fidelity in microphone design, achieving its optimal balance is essential to ensure peak performance across diverse applications.[17–21]

Acknowledging the crucial role of boundary conditions around flow sensors, this article demonstrates how these conditions, which lead to unwanted damping, affect the thermal noise floor and acoustic response. While a typical approach for creating flow sensors involves fabricating sensing elements that extend perpendicularly from a substrate for anchorage, this method is hindered by fabrication

a)Email: mkarimi3@binghamton.edu
b)Email: miles@binghamton.edu

challenges, fragility, and integration issues. In response, the study proposes an alternative packaging method in which the sensor is integrated into a silicon chip for protection. However, this integration introduces boundary conditions from the substrate, which compromise sensor performance. To address this, the substrate is removed by relocating the sensing element to a specially designed cavity (3400 μm length, 1690 μm width, and 500 μm depth). This process eliminates surrounding material, allowing for a direct comparison of sensor performance before and after substrate removal. Although the study includes examples not optimized as flow sensors, they serve to illustrate the significant impact that boundary conditions, particularly those from the substrate, have on sensor behavior. All experiments were conducted in the controlled environment of the anechoic chamber at Binghamton University to ensure precise data collection. The experimental results revealed that removing the substrate increases the viscous damping coefficient of the surrounding air, which reduces thermal noise. At the same time, it reduces damping from the substrate boundaries, thereby improving the acoustic response. This combined effect results in lower PRN levels and a higher signal-to-noise ratio. Ultimately, these modifications reduce the thermal noise floor and enhance the acoustic response, offering significant implications for improving the performance and sensitivity of low-noise detection systems.

II. MATHEMATICAL FORMULATION

Many animals, such as mosquitoes and spiders, detect sounds through hairs that respond to air movement rather than through eardrums sensitive to pressure changes. This natural mechanism provides a lasting source of inspiration for designing innovative acoustic sensors.[22–24] These hairs detect fluid motion due to the interaction between the hair and the airflow, resulting in a viscous force on the hair proportional to the relative velocity between the fluid and the hair. If we consider and simplify a flow-sensing hair, or a microcantilever beam as a single degree of freedom system, as illustrated in Fig. 1, the response can be described using an equation that incorporates a spring, mass, and damper, driven by motion at the end of another damper. The left damper represents viscous damping arising from substrate boundary restrictions, while the right damper represents viscous damping arising from the interaction between the sensing beam and the surrounding air. The former is considered detrimental and "bad" damping as it restricts the motion of the sensing structure in response to sound. In contrast, the latter is considered beneficial and "good" damping as it acts as the primary driving force for the acoustic motion of the beam. This equation governs the motion, x(t), of the system:[15]

$$m\ddot{x} + (c_b + c_g)\dot{x} + kx = c_g\dot{y}, \tag{1}$$

where m represents the mass and k is stiffness. c_b is the bad damping constant that impedes the mass from moving, while c_g is the equivalent viscous damping constant, referred to as good damping, which facilitates the mass movement. $y(t) = Y\sin(\omega t)$ represents the displacement of the fluid, where ω is the excitation frequency and t represents time. By substituting the derivative of fluid displacement, $\dot{y}(t)$, into Eq. (1), the equation is transformed into the following form:

$$m\ddot{x} + (c_b + c_g)\dot{x} + kx = c_gY\omega\cos(\omega t) = F\cos(\omega t). \tag{2}$$

Here, the amplitude of the driving force, denoted as F, is defined as $F = c_gY\omega$. The solution is obtained by expressing it in the form of an amplitude X and a phase θ as follows:

$$\begin{aligned} &x(t) = X\cos(\omega t - \theta),\\ &X = \frac{F/m}{\sqrt{\left(\omega_0^2 - \omega^2\right)^2 + (2\omega_0\zeta\omega)^2}}, \quad F = c_gY\omega,\\ &\theta = \tan^{-1}\left(\frac{2\zeta\omega_n\Omega}{\omega_0^2 - \omega^2}\right),\\ &\zeta = \frac{c_b + c_g}{2\sqrt{km}}, \quad \omega_0 = \sqrt{\frac{k}{m}}, \end{aligned} \tag{3}$$

where ζ represents the damping ratio and ω_0 is the natural frequency in radians per second.

A. Acoustic response

To respond to sound, it is necessary to compare the absolute value of the velocity of the mass, $\dot{x}(\mathrm{t}) = -X\omega\sin(\omega t)$,

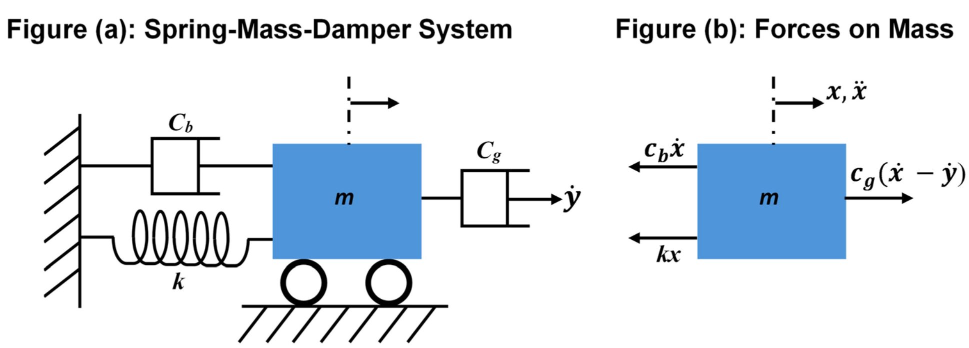

FIG. 1. The forced vibration of a cantilever beam under thermal excitation from the surrounding air. (a) A simplified analytical model of the system. (b) A diagram showing the forces acting on the mass in the horizontal direction when disturbed to the right.

https://doi.org/10.1121/10.0036459

to the velocity of air, $\dot{y}(t) = Y\omega\cos(\omega t)$. By substituting the velocity of the mass and air into Eq. (3), the following acoustic response is obtained (for more information, see Ref. 15):

$$\left|\frac{V}{V_{air}}\right| = \left|\frac{\dot{x}}{\dot{y}}\right| = \left|\frac{-X\omega}{Y\omega}\right| = \left|\frac{X}{Y}\right| = \frac{\frac{c_g\omega}{m}}{\sqrt{\left(\omega_0^2-\omega^2\right)^2+(2\omega_0\zeta\omega)^2}}. \tag{4}$$

Figure 2 presents the acoustic response transfer function between the moving mass and the driving air versus frequency. In Fig. 2(a), a constant $C_g = 1\times 10^{-4}$ is maintained while C_b varies, whereas Fig. 2 (b) maintain a constant $C_b = 1\times 10^{-4}$ with varying C_g values. When the bad damping coefficient is increased while the good damping coefficient is maintained at a reasonable level, the Q-factor of the resonance decreases due to higher damping, reducing the acoustic response near the resonance frequency. Conversely, increasing the good damping coefficient while keeping the bad damping coefficient low enhances the acoustic response across the frequency range.

B. Thermal noise floor

Considering the dominance of a single degree of freedom in the system's motion, the mean square response $E[x^2]$ induced by thermal excitation correlates with the absolute temperature T, according to the equipartition theorem, as follows (for more information, see Ref. 15):

$$\frac{1}{2}K_bT = \frac{1}{2}kE[x^2]. \tag{5}$$

Here, $K_b = 1.38\times 10^{-23}\,\mathrm{m^2\,kg/(s^2}K)$ represents Boltzmann's constant. If $F(t)$ is a weakly stationary random process with two-sided power spectral density S_{FF} with units of $\mathrm{N^2/(rad/s)}$,

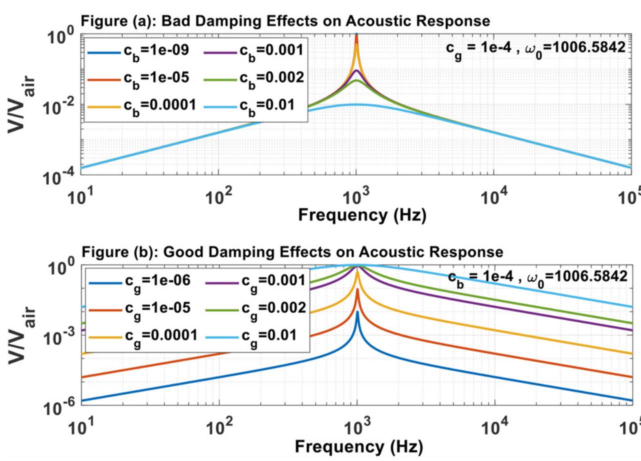

FIG. 2. The effect of damping coefficients on the acoustic response. (a) As the "bad" damping coefficient (C_b) increases, the response near resonance decreases, indicating reduced sensitivity. (b) In contrast, increasing the "good" damping coefficient (C_g) improves the acoustic response across the frequency range, highlighting the positive effect of good damping on sensitivity.

which is constant at all frequencies, it may be shown that the mean square response is given by the following:[15]

$$E[x^2] = \frac{S_{FF}\pi}{k(c_b+c_g)}. \tag{6}$$

The equivalent power spectral density of the force due to thermal excitation is as follows:

$$S_{FF} = \frac{(c_b+c_g)K_bT}{\pi}. \tag{7}$$

The two-sided power spectral density with units of $\mathrm{m^2/(rad/s)}$ of the mass motion from Eq. (3) is related to that of the driving force by the following:

$$S_{xx}(\omega) = \frac{S_{FF}/m^2}{\left(\omega_0^2-\omega^2\right)^2+(2\omega_0\zeta\omega)^2}. \tag{8}$$

Substituting Eq. (7) into Eq. (8), yields the following:

$$S_{xx}(\omega) = \frac{(c_b+c_g)K_bT/\pi m^2}{\left(\omega_0^2-\omega^2\right)^2+(2\omega_0\zeta\omega)^2}. \tag{9}$$

The two-sided power spectral density of the moving mass velocity with units of $\mathrm{(m/s)^2/(rad/s)}$ due to thermal excitation is obtained as follows:

$$S_{\dot{x}\dot{x}}(\omega) = \frac{(c_b+c_g)K_bT\omega^2/\pi m^2}{\left(\omega_0^2-\omega^2\right)^2+(2\omega_0\zeta\omega)^2}. \tag{10}$$

The single-sided power spectral density of the moving mass velocity with units of $\mathrm{(m/s)^2/(Hz)}$ is as follows:

$$G_{\dot{x}\dot{x}}(f) = 4\pi S_{\dot{x}\dot{x}}(\omega) = \frac{4(c_b+c_g)K_bT\omega^2/m^2}{\left(\omega_0^2-\omega^2\right)^2+(2\omega_0\zeta\omega)^2}. \tag{11}$$

The impact of varying damping coefficients, C_b and C_g, on the thermal noise response power spectrum of the moving mass is shown in Fig. 3. Regardless of which damping coefficient increases while the other is maintained at a reasonable value, the thermal noise response demonstrates an overall increase across frequencies, except within the resonance region.

C. Pressure-Referred Noise (PRN)

Sound detection across a wide range of levels is critical, particularly when aiming to detect very quiet sounds. To achieve this, it is important to understand how design parameters influence the sensor's detection capabilities. For conventional pressure-sensing microphones, this capability is often quantified through metrics such as "minimum detectable pressure" or "PRN." The PRN is a measure of a microphone's sensitivity to the inherent noise within the medium, such as thermal noise, and is a key factor in evaluating sensor performance. PRN is determined by the ratio of mechanical thermal noise to the sensor's acoustic pressure response, which is then multiplied by the acoustic impedance Z. This

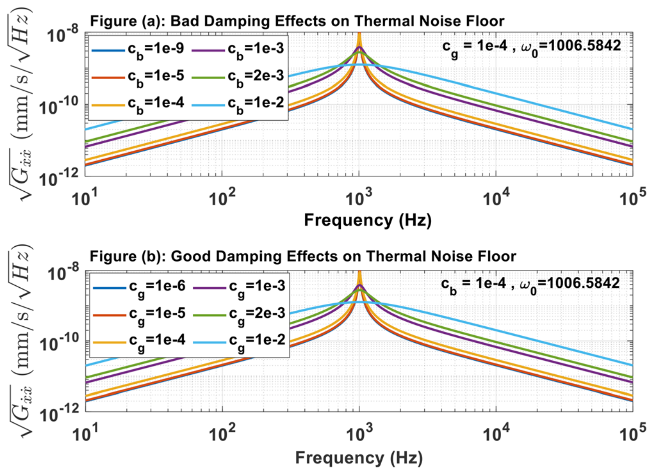

FIG. 3. The effect of damping coefficients on the thermal noise floor. Both damping coefficients have a similar effect on the thermal noise floor: increasing either C_b or C_g while the other is kept constant results in an overall increase in thermal noise response across frequencies, except within the resonance region.

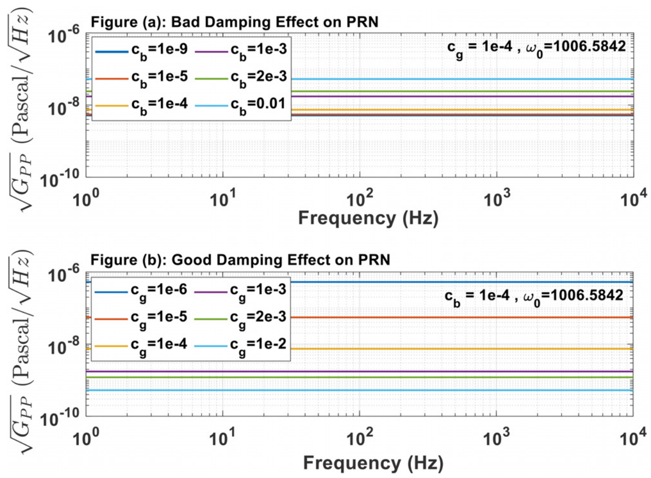

FIG. 4. The effect of damping coefficients on the PRN. Higher values of the "bad" damping coefficient (C_b) increase PRN and reduce sensitivity, whereas increasing the "good" damping coefficient (C_g) decreases PRN, enhancing the system's ability to detect faint sounds.

relationship is captured by Eq. (12), which gives PRN in units of (Pa/$\sqrt{\text{Hz}}$). In this context, P represents the pressure, ρ denotes the density of the medium, and c is the speed of sound in that medium. While both thermal-mechanical noise and acoustic response vary with frequency, PRN tends to remain constant across the audible spectrum. This constancy is because PRN depends more on the uniform characteristics of the microphone's internal components, such as electronic noise from amplifiers or thermal noise from resistors, and the medium's acoustic impedance, rather than the frequency of the sound being detected:

$$\sqrt{G_{PP}} = PRN = \frac{\sqrt{G_{\dot{x}\dot{x}}}}{Acoustic\,Response} \times Z = \frac{\frac{m/s}{\sqrt{Hz}}}{\frac{m/s}{m/s}} \times \frac{pascal}{m/s} = \frac{pascal}{\sqrt{Hz}}, \qquad (12)$$

$$Z = \frac{P}{V_{air}} = \rho c.$$

Figure 4 illustrates how the PRN of the moving mass varies across different frequencies. The data suggest that increasing the bad damping coefficient, while keeping the good damping coefficient within a reasonable range, results in a rise in PRN. This implies that bad damping (C_b) degrades the microphone's performance, reducing its sensitivity to quieter sounds. Conversely, enhancing the good damping coefficient, while keeping the bad damping coefficient at an acceptable level, leads to a decrease in PRN across the frequency spectrum. This indicates that good damping (C_g) improves the microphone's performance by enhancing its ability to detect quieter sounds.

To help clarify the implications of the thermal noise floor and PRN, it is useful to distinguish between them. The "thermal noise response" refers to the inherent motion of the moving mass due to thermal excitation, quantified by the power spectral density of this motion. It describes how thermal energy from the surrounding environment induces random vibrations in the system, which can interfere with the desired signal detection. On the other hand, "PRN" is simply the amount of sound pressure (with units of Pa) that would produce the same response as the thermal noise excitation. It is directly analogous to "input-referred noise" used very commonly in characterizing electronic circuits.

III. EXPERIMENTAL SETUP

All measurements of the thermal noise floor and acoustic response were conducted within the anechoic chamber at Binghamton University. The chamber has interior dimensions of approximately 4.2 m in width, 5.4 m in length, and 3.2 m in height. It is certified by the manufacturer to deliver anechoic conditions for all frequencies above 80 Hz. The verification of this anechoic chamber's performance was carried out in accordance with the methods outlined in ISO Standard 3745-2003, specifically Annex A, which details the general procedures for qualifying anechoic and hemi-anechoic rooms.

Figures 5(a) and 5(b) provide a detailed visualization of the experimental setups for measuring the thermal noise floor and acoustic response. Key components of these setups include a Polytec OFV-534 laser vibrometer, a B&K type 4138 1/8 inch reference microphone, and motorized stages for precise sample positioning. In the acoustic measurement setup, the stimulus signal is generated via MATLAB and transmitted through a National Instruments PXI 1033 data acquisition system. The signal is then processed by a dbx model 234xs crossover filter, which splits it into low, mid-range, and high frequencies. The speaker is 3 m away from the measured location. These signals are amplified by Crown D-75 and Techron 5530 amplifiers and directed to the corresponding woofer, midrange, and tweeter components. The

JASA
https://doi.org/10.1121/10.0036459

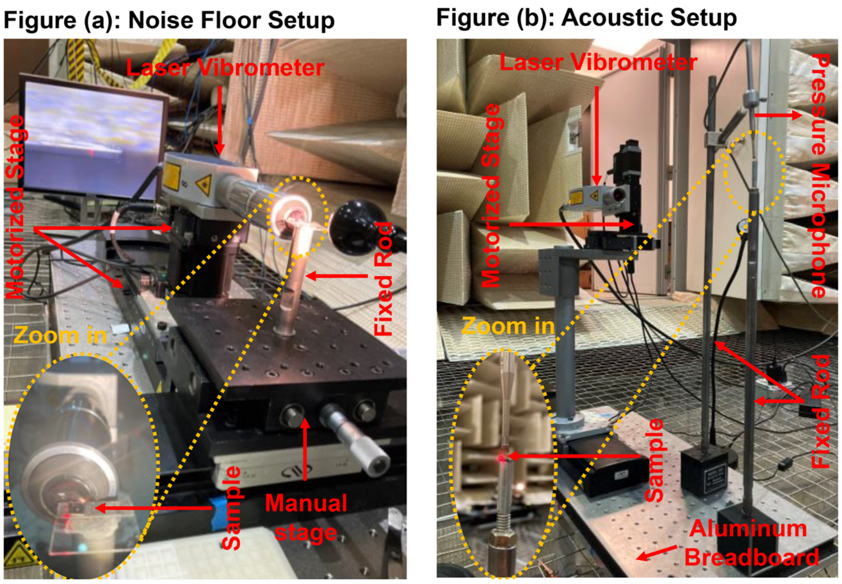

FIG. 5. (a) The thermal noise floor and (b) the acoustic setups, highlighting key components for precise measurement and sample positioning. The system features a Polytec OFV-534 laser vibrometer, B&K type 4138 1/8 inch reference microphone, motorized stages, and an aluminum breadboard platform.

B&K type 4138 microphone records the sound pressure, with its signal further amplified by a B&K type 5935 L dual microphone power supply. Concurrently, the laser vibrometer measures the velocity of the test samples, with data from both instruments collected through the PXI 1033 system.

For the thermal noise floor measurement, the laser vibrometer captures the velocity of the sample caused by thermal excitation. These data are also collected via the PXI 1033 system and analyzed in MATLAB to be plotted.

PRN is calculated using data from both the acoustic response and thermal noise floor. It is determined by the ratio of mechanical thermal noise to the sensor's acoustic pressure response, adjusted by the acoustic impedance Z. This calculation is crucial for assessing the system's sensitivity and is A-weighted over the audio band range of 100 Hz to 40 kHz. For a more detailed discussion on the methodologies for measuring thermal noise floor and acoustic response, refer to Ref. 25.

IV. RESULTS AND DISCUSSION

In this section, the thermal noise floor and acoustic responses of micro cantilever beams with various shapes will be analyzed to illustrate the impact of different fluid boundary conditions. Figures 6(a) and 6(b) show the schematics of a single cantilever beam "with substrate" and the beam "without substrate," respectively. To investigate the influence of various fluid boundary conditions on the beam responses, the thermal noise floor and acoustic tests will initially be performed with all beams positioned approximately 1 μm above the underlying step and around 100 μm from the chip substrate, a setup referred to as the beam "with substrate" [Fig. 6(a)].

To isolate the effects of different fluid boundary conditions on the structure, it is imperative to maintain consistency by utilizing the same sample or beam. To achieve this, the structure will be delicately detached from the current chip and securely affixed onto another chip with a specially designed cavity, thereby completely removing the substrate, including the step, electrodes, and substrate. This setup is referred to as the beam "without substrate" [Fig. 6(b)]. At the end of the experiment, the responses of the beam with and without substrate will be compared to assess the influence of changing fluid boundary conditions.

The depicted cavity selected for transferring process has a length of 3400 μm, a width of 1690 μm, and a depth of

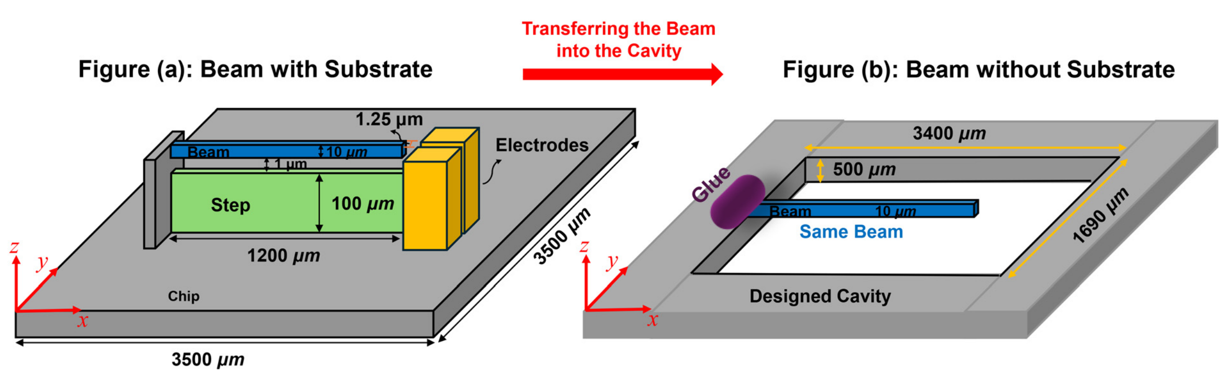

FIG. 6. Schematic of a single cantilever beam (a) "with substrate" and (b) "without substrate." These figures depict the beam mounted on the chip with detailed components, illustrating the process of transferring the beam into the design cavity.

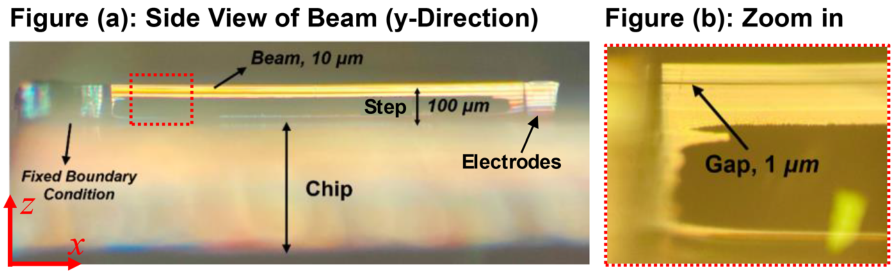

FIG. 7. Side view of a single beam (y direction) showing the hinge connection, step, electrodes, and cantilever beam configuration.

500 μm. The precise transfer process is conducted using a model 525 Micromanipulator, a Leica WILD M3Z Stereo Zoom Microscope, a Zeiss AxioSkop-40 microscope, and super glue. These tools, along with extreme care, will play a crucial role in ensuring the accurate and secure relocation of the structure for further experimentation.

Again, it is worth noting that all beams to be measured at first possess a step with the size of 100 μm from the chip substrate, and they are situated 1 μm above the surface of the wall. To provide additional clarity and visual context, Fig. 7 offers a side view of a single beam, offering a clear depiction of the hinge connection to the fixed boundary condition. It should be mentioned that the selected chip with a single beam for photographing has a damaged wall which can be seen in Fig. 7.

Each type of cantilever beam in our inventory has been assigned a unique name, reflecting the variety of shapes they encompass. The velocity-sensitive microphone is still in the early stages of development, and these different beam shapes have been designed and manufactured with inspiration from nature. The goal is to investigate important parameters that could enhance the sensitivity of these beams. While these designs are not yet optimized, they are being tested to determine the influence of fluid boundary conditions. To initiate the experiment, a straightforward or single cantilever beam was chosen with dimensions: length of 1200 μm (x direction), width of 10 μm (z direction), and thickness of 1.25 μm (y direction) as depicted in Fig. 8(a). The images were acquired using a Nikon Eclipse LV-100D microscope. It is worth noting that the beam vibrates horizontally, which is reflected in its naming convention based on its thickness and width. Following the measurement of this micro single beam, it was delicately and precisely transferred using the Micromanipulator and microscopes to a designated cavity. Through this transferring process, both the substrate and the underlying wall underneath the structures will be removed. This transfer aims to alter the fluid boundary conditions and observe its effects on the thermal noise floor response which is shown in Fig. 8(b).

Figure 9(a) shows the noise floor response before filtration. Since we are primarily interested in the thermal noise response, efforts were made to reduce electromagnetic noise from the instrumentation, which is concentrated at discrete frequencies. This noise can be minimized using filters. Figure 9(b) shows the filtering process, which effectively removes the pure tone from the signal. From this point onward, only the filtered results will be shown to ensure clarity and avoid redundancy.

Figure 10(a) shows the thermal noise floor response of cantilever beams with and without substrate across various frequencies. Based on Fig. 10(a), the first natural frequency for the beam with substrate measures around 1184 Hz, while for the beam without substrate, it registers at approximately 1283 Hz. To investigate the accuracy of the results, the experimental results must be compared with other methods, such as theoretical methods. The first natural frequency of a cantilever beam can be determined using the formula $f=(3.52/2\pi)\sqrt{(EI/(\rho A l^4))}$, where, E, I, l, ρ, and A represent

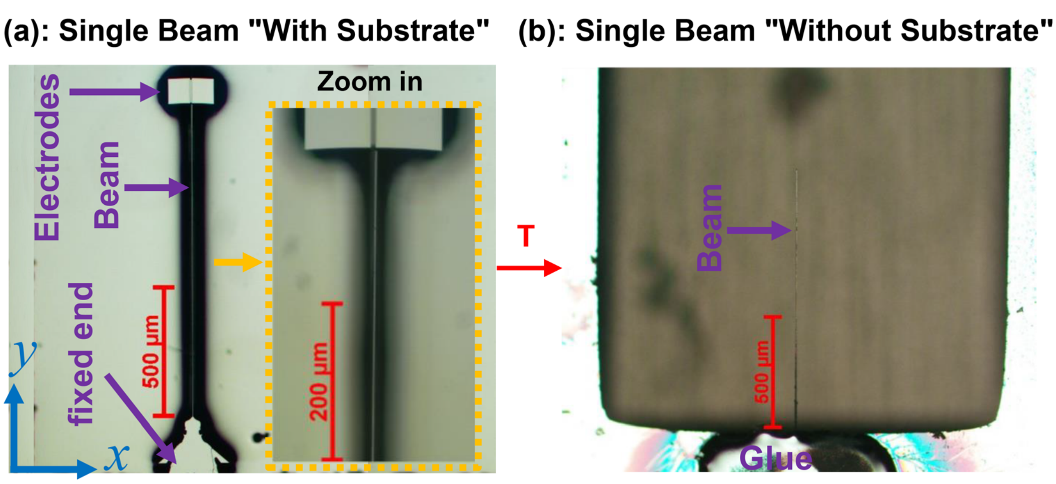

FIG. 8. Single micro cantilever beam (a) "with substrate" and (b) "without substrate." The photos are in the Z direction. "T" indicates the transfer of the beam to the cavity.

https://doi.org/10.1121/10.0036459

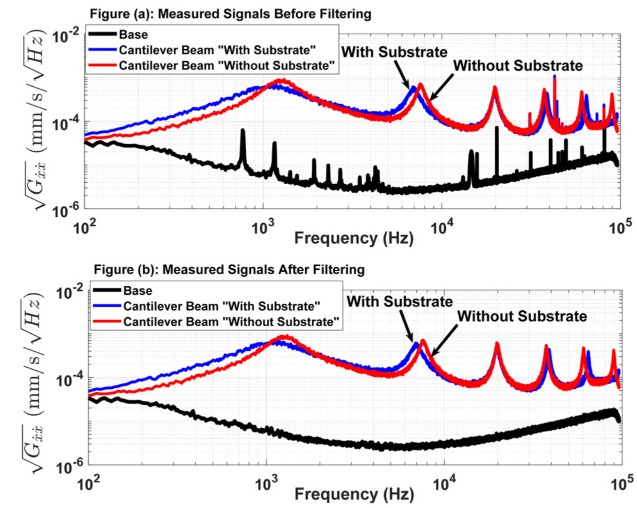

FIG. 9. The filtering process that effectively removed unwanted noise from the signal. (a) Measured signals before applying filtering. (b) Measured signals after applying filtering.

the modulus of elasticity, area moment of inertia, beam length, density, and cross-sectional area, respectively.[26] For comparison between the experimental and theoretical results, the structures are fabricated using a silicon on insulator wafer, so that the device consists of single crystal silicon with modulus of elasticity $E = 170\,\mathrm{GPa}$ and density $\rho = 2329\,\mathrm{kg/m^3}$. Additionally, the dimensions of the cantilever beam are $h = 1.25\,\mu\mathrm{m}$, $b = 10\,\mu\mathrm{m}$, and $l = 1200\,\mu\mathrm{m}$. Using the theoretical formula with the given values, the experimental method for the beam with substrate yielded a first natural frequency of 1184 Hz, while the theoretical method predicted a value of 1199.4 Hz. These results show close agreement between the predictions and the measurements.

Returning to the analysis of the results presented in Fig. 10(a), during the transfer process to the specified cavity, the beam experienced a break at the hinge. This event resulted in a shorter beam, subsequently causing an increase in its natural frequency. This increase is clearly observed in the results for the beam without substrate and can be estimated using the previously mentioned formula for natural frequency. Similarly, using the formula $f = (1/2\pi)\sqrt{(K/\mathrm{m})}$ outlines an equivalent spring-mass system for a beam to calculate its natural frequency.[26] In this formula, "K" represents beam stiffness, and "m" stands for the effective mass. According to this formula, decreasing the effective mass and increasing the stiffness (achieved by shortening the beam) both contribute to an increase in the natural frequency.

Additionally, the observed rise in resonance frequency after substrate removal can also be attributed to the reduction in the effective air mass load on the beam. It is well established that reducing the air mass load increases the resonance frequency of mechanical structures and affects their Q-factor.[27] This dual effect (shortening of the beam and air mass reduction) explains the observed shift toward higher natural frequencies. This phenomenon has been consistently observed across various cantilever beam shapes, and the detailed results will be presented in this paper.

The pivotal observation derived from Fig. 10(a) is the overall decrease in the thermal noise floor level across frequencies, up to the second mode (7 kHz), except for the resonance region after transferring to the cavity, henceforth referred to as the beam "without substrate." Additionally, the first natural frequency peak of the cantilever becomes sharper and narrower after the transfer, which corresponds to an increase in the Q-factor. This phenomenon was also observed and predicted in the theoretical model depicted in Fig. 3, providing validation for our experimental measurements.

This observation indicates a reduction in the influence of bad damping (C_b) on the cantilever beam with substrate. To elaborate further, when the beam with substrate is situated on the chip, the gap between the cantilever beam and the step is approximately 1 μm. This proximity results in air molecules being more densely packed, which increases the viscous boundary layer effect between the beam and the surrounding air. In turn, this creates more contact between the beam with substrate and air molecules, intensifying the damping effect on the beam and increasing the bad damping coefficient (C_b). As a result, the first natural frequency peak becomes more diffused and broader, which can be attributed to the elevated air damping coefficient, corresponding to a lower Q-factor.

In contrast, when the beam without substrate is positioned within the cavity, there is no substrate beneath it, creating a 500-μm gap between the beam and the surface. This allows air molecules to move more freely and expand, reducing their contact with the beam and decreasing the thickness of the viscous boundary layer. This reduction in proximity effects, coupled with the smaller viscous boundary layer, leads to a decrease in the bad damping coefficient (C_b). As a result, the reduction in air damping and the altered proximity effects cause the first natural frequency peak to become sharper and narrower, which is associated with an increase in the Q-factor.

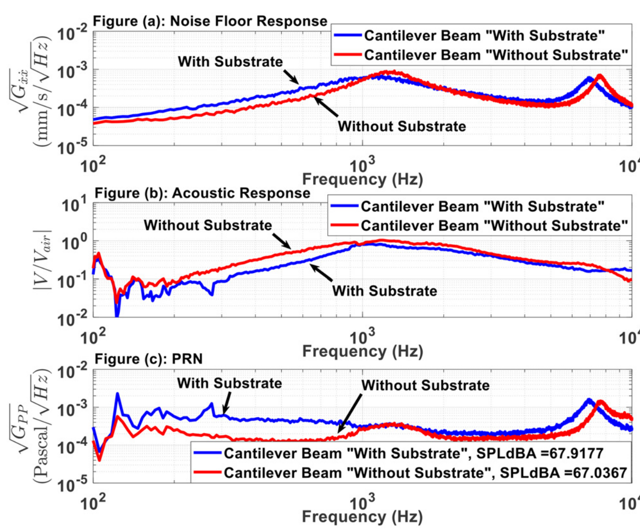

FIG. 10. Comparison of (a) thermal noise floor response, (b) acoustic response, and (c) PRN of cantilever beam with and without substrate versus frequency.

It is worth noting that, due to the narrowness of the cantilever beam, the effects of changes in fluid boundary conditions (e.g., the removal of the substrate) and the corresponding alterations in the viscous boundary layers and proximity effects may be less pronounced compared to larger structures. Larger structures would more effectively demonstrate the impact of these changes in fluid boundary conditions, viscous boundary layer thickness, and proximity

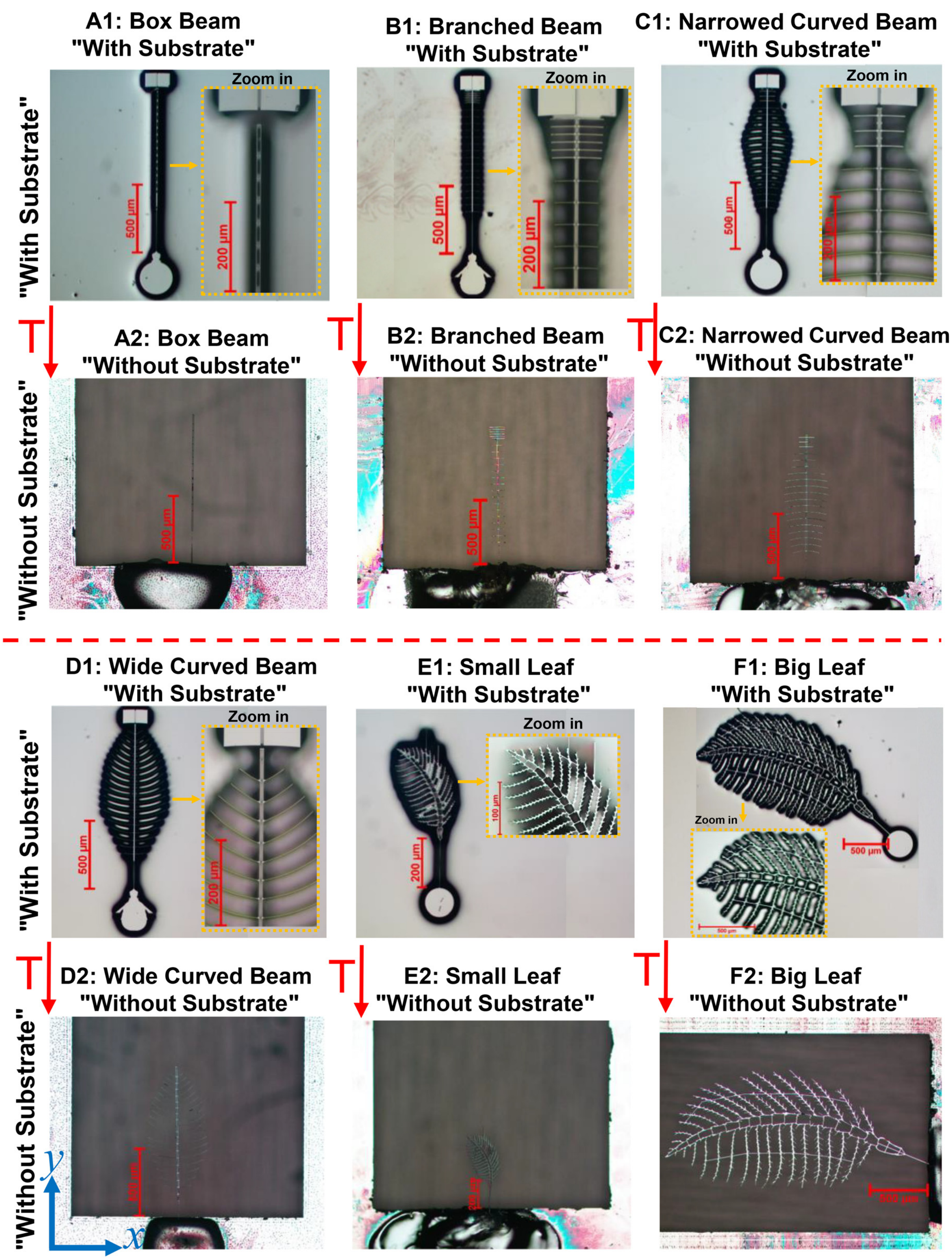

FIG. 11. Various shapes of microcantilever beams. Symbol 1 denotes beams with substrate, while Symbol 2 denotes beams without substrate. The photos are in the z direction. "T" indicates the transfer of the beam to the cavity. The anchorage location, or fixed end, for all of the beams is at the bottom, where the beam is attached to a circular-shaped base.

https://doi.org/10.1121/10.0036459

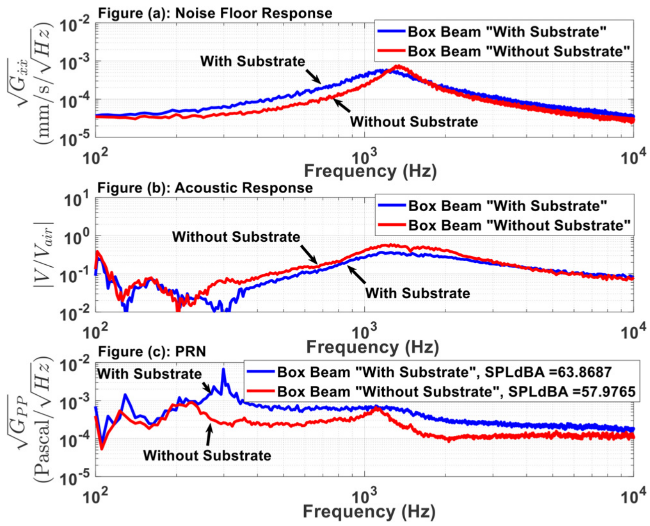

FIG. 12. Comparison of (a) thermal noise floor response, (b) acoustic response, and (c) PRN of box beam with and without substrate versus frequency.

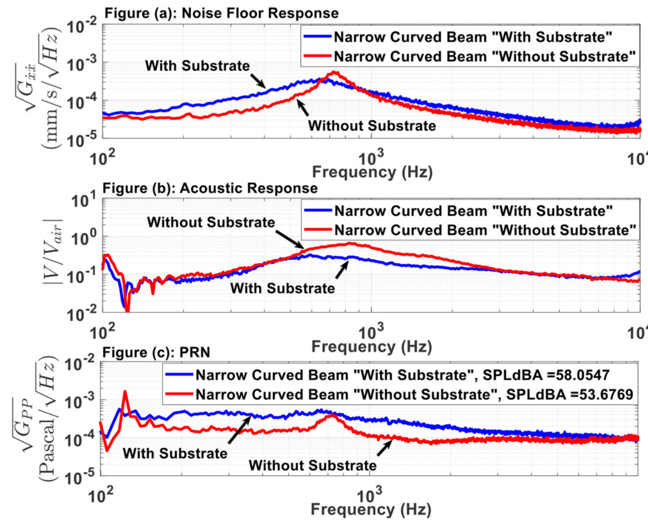

FIG. 14. Comparison of (a) thermal noise floor response, (b) acoustic response, and (c) PRN of narrow curved beam with and without substrate versus frequency.

effects on the thermal noise floor response, which will be further explored in the subsequent discussion.

Figures 10(b) and 10(c) illustrate the impact of fluid boundary conditions on the acoustic response and PRN of cantilever beams, with and without substrate, across various frequencies, respectively. The frequency range spans from 100 Hz to 40 kHz, which is the frequency range of interest.

In Fig. 10(b), it can be observed that the acoustic response of the micro cantilever beam increases after transferring to the designated cavity, referred to as cantilever beams without substrate. Eliminating the backside boundary conditions frees the sensing beam from stagnant air, thereby increasing its interaction with sound-induced air motion. Consequently, the damping coefficient from the driving air, C_g is effectively enhanced. This observation aligns with the predictions of the simplified analytical model, demonstrating an increase in acoustic response across the frequency range.

To design effective acoustic velocity sensors, it is crucial to understand their sensitivity to thermal noise in the medium, which is why Fig. 10(c) was plotted. Figure 10(c) illustrates that the PRN for the beam without substrate is lower than that of the one with substrate. This improved performance is attributed to a higher Q-factor, indicating reduced energy losses. This suggests that the beam without substrate is more effective in sensing quieter sounds compared to the one with substrate.

In Fig. 10(c) and all subsequent figures related to PRN, the calculation of SPL dBA is critical for assessing the system's sensitivity. SPL dBA values are calculated using an

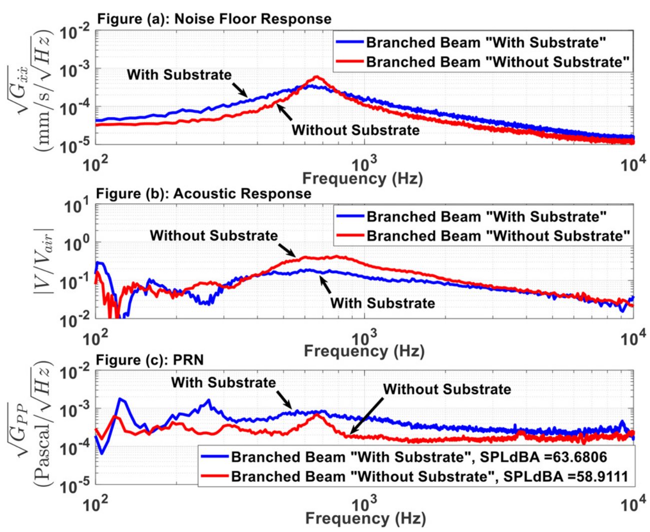

FIG. 13. Comparison of (a) thermal noise floor response, (b) acoustic response, and (c) PRN of branched beam with and without substrate versus frequency.

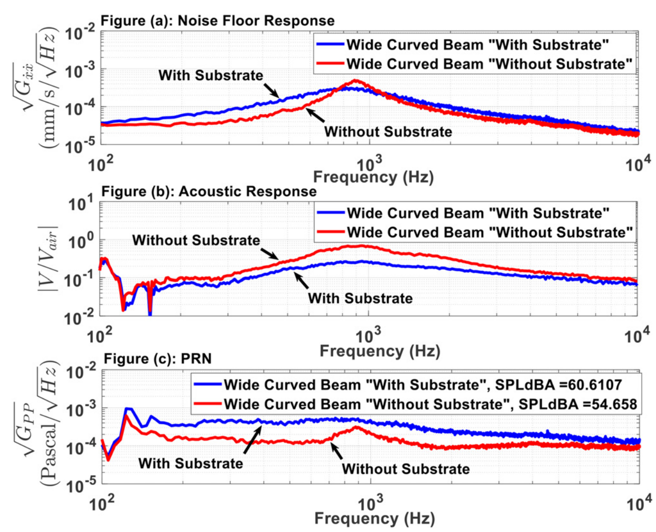

FIG. 15. Comparison of (a) thermal noise floor response, (b) acoustic response, and (c) PRN of wide curved beam with and without substrate versus frequency.

https://doi.org/10.1121/10.0036459

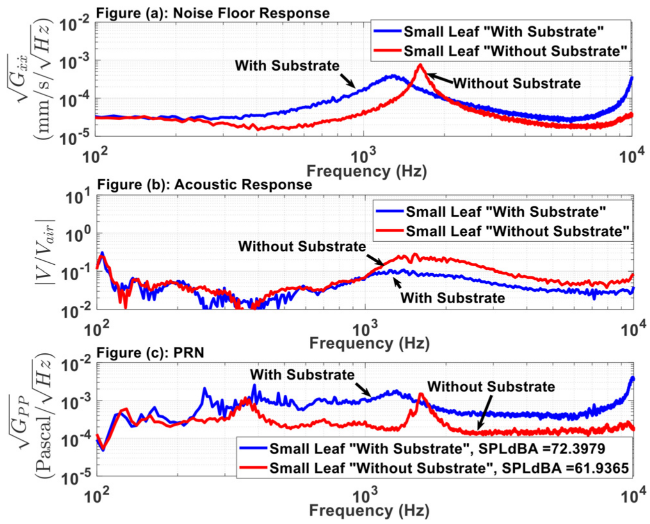

FIG. 16. Comparison of (a) thermal noise floor response, (b) acoustic response, and (c) PRN of small leaf with and without substrate versus frequency.

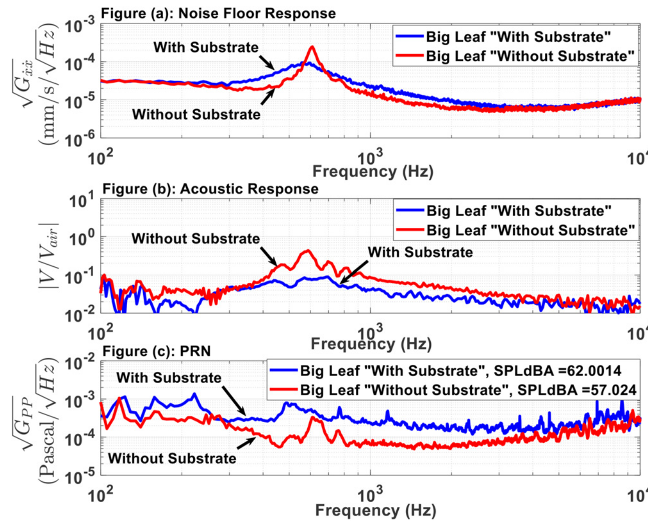

FIG. 17. Comparison of (a) thermal noise floor response, (b) acoustic response, and (c) PRN of big leaf with and without substrate versus frequency.

A-weighting filter over the audio band range of 100 Hz to 40 kHz.

To ensure the validity and accuracy of the results, it is essential to conduct the same experiment on different shapes of cantilever beams. Figures 11(a)–11(f) present various shapes of microcantilever beams, including "box beams," "branched beams," "narrow curved beams," "wide curved beams," "small leaf," and "big leaf," respectively. Each shape is shown for both configurations: beams "with substrate" and beams "without substrate." It is worth noting that the designs of these structures are inspired by nature itself. Nature has always been a profound source of inspiration, as it continually evolves and adapts to overcome challenging environments. These biomimetic designs reflect an effort to harness the ingenuity and efficiency of natural forms for scientific exploration and innovation.

Figures 12–17 present the measurement results for these beam shapes in the same order as shown in Fig. 11. Similar results have been observed across these figures; and for the sake of brevity, the main points will be highlighted without repeating the underlying reasons.

From Figs. 12(a)–17(a), it can be observed that the beam without substrate demonstrates an overall decrease in the thermal noise floor level across frequencies, except for the resonance region. This suggests a reduction in the bad damping coefficient (C_b), which is associated with an increase in the Q-factor. The first natural frequency of these beams is presented in Table I. Additionally, the results for the single beam are included in this table to provide a comprehensive comparison.

From Figs. 12(b)–17(b), the beam without substrate displays a heightened acoustic response compared to the one with substrate, suggesting a reduction in bad damping upon removal of the substrate.

Additionally, in Figs. 12(c)–17(c), it is observed that the PRN associated with the beam without substrate is at a lower level in contrast to the one with substrate. The SPL dBA for the different beams with and without substrate over the range of 100 Hz to 40 kHz is presented in Table II. From this table, the "narrow curved" beam has the lowest SPL dBA for both the beam with and without substrate compared to other beam shapes. This indicates that "narrow curved" beam has better performance and can detect quieter sounds.

Moreover, it becomes clear that increasing the surface area of the structures, such as transitioning from a single beam to a more complex configuration, amplifies the impact of removing the substrate on the beam's behavior. This is attributed to the enhanced interaction between air molecules and the larger surface area of the beam with substrate. As a result, the larger beam moves through a denser arrangement of air molecules, leading to an increase in the air damping coefficient. In contrast, when the beam without substrate is placed within the cavity, its larger surface area interacts with air molecules that have greater freedom of movement. Consequently, the shift from a beam with substrate to one without substrate has a more significant effect on the beam

TABLE I. First natural frequencies of different beam shapes, with and without substrate.

Beam specification	Single beam (Hz)	Box beam (Hz)	Branched beam (Hz)	Narrow curved beam (Hz)	Wide curved beam (Hz)	Small leaf (Hz)	Big leaf (Hz)
With substrate	1184	1202	639	656	867	838	568
Without substrate	1283	1342	668	732	896	932	609

TABLE II. SPL dBA for different beam shapes across the continuous frequency range of 100 Hz to 40 kHz, with and without substrate.

Beam specification	Single beam	Box beam	Branched beam	Narrow curved beam	Wide curved beam	Small leaf	Big leaf
With substrate	67.92	63.87	63.68	58.05	60.61	72.40	62.00
Without substrate	67.04	57.98	58.91	53.68	54.66	61.94	57.02
SPL dBA difference	1	6	5	4.5	6	10	5

with the larger surface area, highlighting the pronounced influence of the altered environment. From Table II, this shift is more evident in the "small leaf," where the SPL dBA difference between the beam with and without substrate is around 10.

Overall, these findings suggest that a beam without substrate is more effective in sensing quieter sounds compared to one with a substrate.

V. CONCLUSION

In this study, an extensive experimental investigation was conducted to analyze the influence of different fluid boundary conditions on the thermal noise floor response, acoustic response, and PRN of various microcantilever beam configurations. The measurements were meticulously conducted within the controlled environment of the anechoic chamber at Binghamton University, ensuring the highest level of data accuracy. A simplified analytical model predicted the effect of different viscous damping from the fluid boundary condition (bad damping, C_b) and fluid itself (good damping, C_g) on structural dynamic response due to thermal-mechanical noise and acoustic excitation. A practical approach was developed to modify the fluid boundary conditions by exploring various microcantilever shapes and removing the substrate. The substrate was successfully removed by transferring the sensing element into a specially designed cavity, eliminating surrounding material and enabling a direct comparison of the sensor's performance before and after substrate removal.

The results indicated that the beam without substrate exhibited a general reduction in the thermal noise floor level across frequencies, with the exception of the resonance region. This implies a decrease in the bad damping coefficient (C_b), which correlates with an increase in the Q-factor.

Moreover, the findings confirmed that reducing bad damping (C_b) by removing the substrate leads to a reduction in the thermal noise level of the flow sensor, while simultaneously increasing its acoustic response. Overall, this results in a decrease in PRN and a consequent improvement in the performance of the acoustic sensor.

Additionally, the study underscored the crucial role of structural size, with larger surface areas demonstrating a more pronounced sensitivity to variations in fluid boundary conditions. As the size of the beam increased, the interaction between air molecules and the beam's surface intensified, amplifying the influence of the altered environment.

Overall, these findings offer significant potential for advancing low-noise acoustic flow sensors, where reducing PRN is critical for detecting faint signals.

ACKNOWLEDGMENTS

Research reported in this publication was supported by National Institute on Deafness and Other Communication Disorders of the National Institutes of Health Award No. R01DC017720 to R.N.M. The fabrication of various shapes of microcantilevers was performed in part at the Cornell NanoScale Facility, an NNCI member supported by National Science Foundation Grant No. NNCI-2025233.

AUTHOR DECLARATIONS

Conflict of Interest

The authors have no conflicts to disclose.

DATA AVAILABILITY

The data that support the findings of this study are available within the article.

[1]S. K. Vashist, "A review of microcantilevers for sensing applications," J. Nanotechnol. **3**, 1–18 (2007).
[2]S. K. Vashist and H. Holthöfer, "Microcantilevers for sensing applications," Meas. Control **43**, 84–88 (2010).
[3]M. A. Razzaq, R. T. Rocha, Y. Tian, S. Towfighian, S. F. Masri, and M. I. Younis, "Nonparametric identification of a MEMS resonator actuated by levitation forces," Int. J. Non-Linear Mech. **160**, 104633 (2024).
[4]F. Najar, M. Ghommem, and A. Abdelkefi, "A double-side electrically-actuated arch microbeam for pressure sensing applications," Int. J. Mech. Sci. **178**, 105624 (2020).
[5]Z. Dong, J. Li, X. Wang, Y. Liu, and C. Pan, "A flexible flow sensor for detecting airflow velocity and incident angle," IEEE Sens. J. **22**, 15884–15892 (2022).
[6]Z. Shadmand, J. R. Shahrouzi, and H. H. Chaboki, "Design and fabrication of a graphene-based microcantilever flow sensor for liquid flow measurement," Sens. Actuators A **317**, 112438 (2021).
[7]M. Madadi and P. Zhang, "Finite-size effect on the percolation and electromechanical behaviors of liquid metal particulate composites," Soft Matter **20**, 1061–1069 (2024).
[8]A. N. Cleland and M. L. Roukes, "Noise processes in nanomechanical resonators," J. Appl. Physiol. **92**, 2758–2769 (2002).
[9]J. R. Vig and Y. Kim, "Noise in microelectromechanical system resonators," IEEE Trans. Ultrason. Ferroelectr. Freq. Controlled **46**, 1558–1565 (1999).
[10]F. Mohd-Yasin, D. J. Nagel, and C. E. Korman, "Noise in MEMS," Meas. Sci. Technol. **21**(1), 012001 (2009).
[11]P. Durdaut, S. Zabel, G. Gerlach, M. Wurz, H. Seidel, and E. Quandt, "Thermal-mechanical noise in resonant thin-film magnetoelectric sensors," IEEE Sens. J. **17**, 2338–2348 (2017).
[12]B.-H. Kim and H.-S. Lee, "Acoustical-thermal noise in a capacitive MEMS microphone," IEEE Sens. J. **15**, 6853–6860 (2015).
[13]J. D. Smith, *Thermal Noise in Electronic and Mechanical Devices* (Wiley, New York, 2008).
[14]V. Michaud-Belleau, E. R. N. Fokoua, P. Horak, N. V. Wheeler, S. Rikimi, T. D. Bradley, and R. Slavík, "Fundamental thermal noise in anti-resonant hollow-core fibers," Phys. Rev. A **106**, 023501 (2022).
[15]R. N. Miles, *Physical Approach to Engineering Acoustics* (Springer, New York, 2020).

[16]T. Gabrielson, "Mechanical-thermal noise in micromachined acoustic and vibration sensors," IEEE Trans. Electron Devices **40**, 903–909 (1993).
[17]P. Fellgett, "Thermal noise limits of microphones," J. Inst. Electron. Radio Eng. **57**, 161–166 (1987).
[18]R. Miles and J. Zhou, "Sound-induced motion of a nanoscale fiber," J. Vib. Acoust. **140**, 011009 (2018).
[19]J. Zhou, B. Li, J. Liu, W. E. Jones, Jr., and R. N. Miles, "Highly-damped nanofiber mesh for ultrasensitive broadband acoustic flow detection," J. Micromech. Microeng. **28**, 095003 (2018).
[20]J. Zhou and R. N. Miles, "Sensing fluctuating airflow with spider silk," Proc. Natl. Acad. Sci. U.S.A. **114**, 12120–12125 (2017).
[21]J. Lai, M. Farahikia, M. Karimi, Z. Liu, Y. Jiang, C. Ke, and R. Miles, "Effect of size on the thermal noise and acoustic response of viscous-driven microbeams," J. Acoust. Soc. Am. **155**, 2561–2576 (2024).
[22]R. Miles, "Most animals hear acoustic flow instead of pressure; we should too," J. Acoust. Soc. Am. **145**, 1698 (2019).
[23]L. Díaz-García, B. Latham, A. Reid, and J. Windmill, "Review of the applications of principles of insect hearing to microscale acoustic engineering challenges," Bioinspir. Biomim. **18**(5), 051002 (2023).
[24]J. Zhou, J. Lai, G. Menda, J. A. Stafstrom, C. I. Miles, R. R. Hoy, and R. N. Miles, "Outsourced hearing in an orb-weaving spider that uses its web as an auditory sensor," Proc. Natl. Acad. Sci. U.S.A. **119**, e2122789119 (2022).
[25]J. Lai, M. Karimi, and R. Miles, "Methods for accurate acoustic characterization with ultra-low noise and minimal effect from acoustic reflections," Engineering Archive (2023).
[26]M. I. Younis, *MEMS Linear and Nonlinear Statics and Dynamics* (Springer, New York, 2011).
[27]V. Naderyan, R. Raspet, and C. Hickey, "Analytical, computational, and experimental study of thermoviscous acoustic damping in perforated micro-electro-mechanical systems with flexible diaphragm," J. Acoust. Soc. Am. **150**, 2749–2756 (2021).